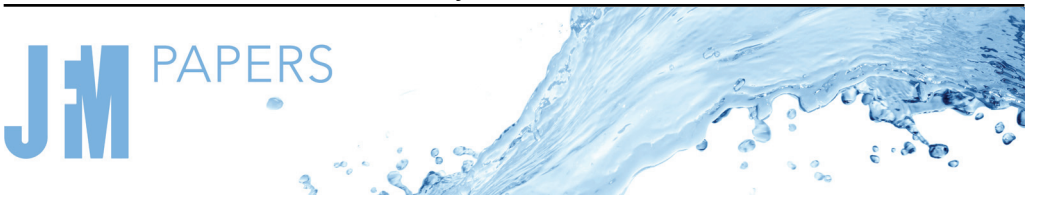
*J. Fluid Mech.* (2026), *vol.* 1026, A5, doi:10.1017/jfm.2025.10961



# Negative differential flow resistance in reverse osmosis

**Fan Li**[1], **Ziheng Wang**[1] **and Yanbo Xie**[2]

[1]School of Physical Science and Technology, Northwestern Polytechnical University, Xi'an 710072, PR China

[2]School of Aeronautics and Institute of Extreme Mechanics, Northwestern Polytechnical University, Xi'an 710072, PR China

**Corresponding author:** Yanbo Xie, ybxie@nwpu.edu.cn

(Received 17 May 2025; revised 15 September 2025; accepted 11 November 2025)

Reverse osmosis (RO) is an efficient desalination approach, but the widely used solution-diffusion model was challenged for failing to explain field-dependent permeabilities, particularly when the continuum theory may break down in Ångström scale. Here we developed a non-equilibrium statistical theory, supported by molecular dynamics simulations that captures the field-dependent water and ion permeabilities through a single Ångström-scale channel. Surprisingly, our simulation reveals a counterintuitive negative differential flow resistance (NDFR) effect, where the flow velocity decreases with increasing pressure. This phenomenon arises from ion trapping at the nanotube entrance, caused by dielectric and dehydration barriers and hydrodynamic friction. The NDFR effect significantly reduces water permeability and may be a predominant factor constraining the selectivity-permeability trade-off in RO. Our statistical theory is based on a bidirectional escape framework that predicts the pressure- and size-dependent permeabilities and explains the NDFR effect. Our findings offer molecular-level insights into RO and can be extended to broader transport phenomena in confined systems.

**Key words:** coupled diffusion and flow, non-continuum effects, microscale transport

## 1. Introduction

Reverse osmosis (RO) shows its high efficiency (Greenlee *et al.* 2009; Park *et al.* 2017; Zuo *et al.* 2020; Di Vincenzo *et al.* 2021; DuChanois *et al.* 2022; Yao *et al.* 2024) and promising features in desalination (Fornasiero *et al.* 2008) and energy applications (Siria *et al.* 2013; Janssen *et al.* 2014; Macha *et al.* 2019; Zhang, Wen & Jiang 2021; Baldock & Huang 2024). Ions are rejected by the steric repulsion, dehydration or dielectric energy barrier at the membrane, enabling water to permeate, thus removing hydrated ions from

© The Author(s), 2025. Published by Cambridge University Press.



https://doi.org/10.1017/jfm.2025.10961 Published online by Cambridge University Press

electrolyte solution via pressure-driven flows across the membrane. The solution-diffusion (SD) model is the most widely used theory to describe the water and ion permeation through the membrane (Paul 1973; Wijmans & Baker 1995). However, recent studies showed ions are permeable through membranes when the pressure gradient exceeds a threshold (Zhang *et al.* 2020; Wang *et al.* 2021, 2023; Biesheuvel *et al.* 2023), which is also influenced by salt concentration (Straub *et al.* 2015; Biesheuvel *et al.* 2022), thereby compromising desalination selectivity. Besides, water flux has a nonlinear response to the applied pressure (Zhou & Song 2005; Xu *et al.* 2019; Yong *et al.* 2022). These pressure-dependent permeations deviate from the constant that was predicted by the SD model.

The core assumptions of the SD model were challenged with evidence of Ångström-scale pores in membrane (Fujioka *et al.* 2015; Culp *et al.* 2021; Foglia *et al.* 2022), which have limitations in describing permeation behaviours (Sahu *et al.* 2017; Qasim *et al.* 2019; Wang *et al.* 2021; Lu *et al.* 2023; Nickerson *et al.* 2023; Fan *et al.* 2024). Hence, new theoretical frameworks, including the pore-flow model (Sarbolouki & Miller 1973; Takeuchi *et al.* 2018; Hegde, Doherty & Squires 2022; Geise 2022) based on an extended Nernst–Planck equation and the solution-friction model (Wang & Lin 2021; Wang *et al.* 2021, 2023) based on hydrodynamic friction, were recently developed to explain these deviations. Additionally, coupling between water and ion flux must be considered, as demonstrated by a unified non-equilibrium simulation using a flux matrix under generic forces (Monet, Bocquet & Bocquet 2023).

However, recent studies found 'bizarre' phenomena when pores/channels come to Ångström-scale regime (Bocquet 2020; Kavokine, Netz & Bocquet 2021; You *et al.* 2022; Aluru *et al.* 2023), such as fast transport (Radha *et al.* 2016; Tunuguntla *et al.* 2017), ionic Coulomb blockade (Feng *et al.* 2016; Kavokine *et al.* 2019; Xie *et al.* 2023; Zhang, Fu & Xie 2024), proton transport (Comtet *et al.* 2021) and iontronics (Robin *et al.* 2021, 2023; Shi *et al.* 2023), where continuum theories breakdown (Faucher *et al.* 2019). The molecular-level transport calls for a statistical mechanics framework incorporating molecular thermodynamics for modelling of water and ion permeation (Nickerson *et al.* 2023).

In this work, we used non-equilibrium molecular dynamics (NEMD) to investigate ion and water permeation through a single Ångströmchannel under pressure-driven flow, employing a generic Lennard-Jones (LJ) wall nanotube as a toy model. We found that water and ion permeability are pressure-dependent, with ionic fluxes rapidly increasing beyond a threshold pressure, qualitatively consistent with trends in experiments (Zhang *et al.* 2020; Biesheuvel *et al.* 2023; Wang *et al.* 2021, 2023) but deviating from the constant predicted by the SD model. We identified a negative differential flow resistance (NDFR) phenomenon, where flow velocity decreases with increasing pressure. This NDFR arises from the reduced escape rate of trapped ions at the entrance by joint actions of the energy barrier and hydrodynamic force that provide additional friction in the system. Trapped ions significantly reduce water permeation, emerging as a predominant factor limiting water permeation, even in low-friction systems. Since continuum theories may fail to capture the NDFR behaviour due to neglecting thermodynamic processes, we develop a non-equilibrium statistical theory to describe the ion transport and water flow through an Ångström channel for RO, capturing pressure-dependent permeance and the NDFR phenomenon using phase diagrams as functions of pressure gradient and channel size. Although this NDFR effect may statistically average out in parallel channels with a certain size distribution, the trapped ions still strongly reduce the membrane performance. Our results indicate that even under such ideal conditions, such as neutral and low frictional walls, in Ångström-scale confinement, we observe a strong suppression of water permeability due to the entrance ion trap, suggesting the ion trapping is the intrinsic



https://doi.org/10.1017/jfm.2025.10961 Published online by Cambridge University Press

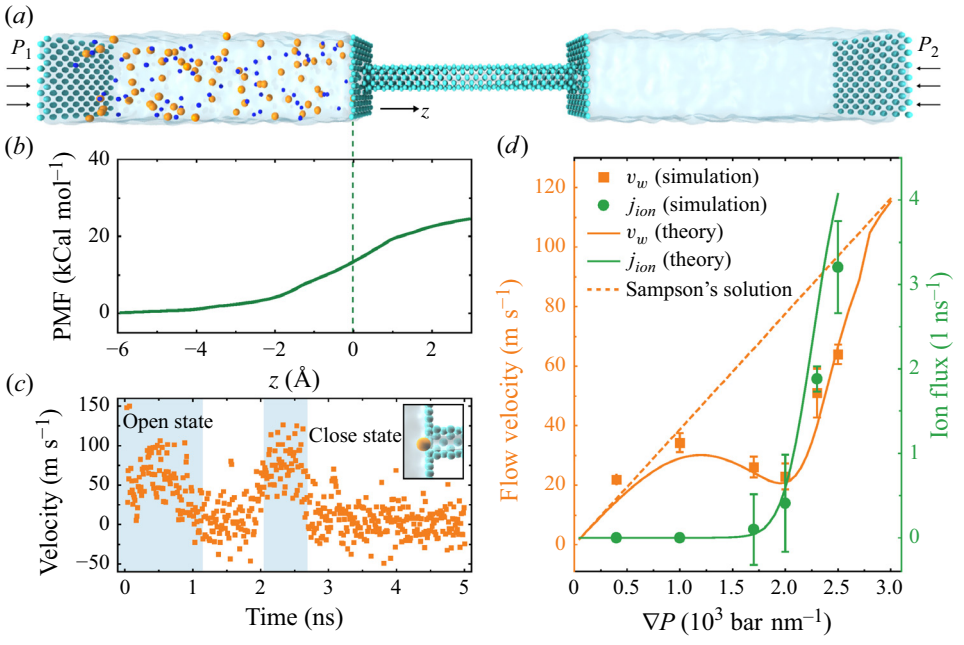



Figure 1. (*a*) Simulation system. Pressures on pistons drive water and ion (blue for $Na^+$, orange for $Cl^-$) transport from the left reservoir through a generic LJ nanotube (cyan) to the right pure water box. Pressures are applied at the pistons, with $P_1$ at left and $P_2$ at right side. (*b*) Averaged PMF for an ion entering the nanotube, with the dashed line marking the nanotube entrance. (*c*) Water flow velocity over time at 2000 bar nm$^{-1}$. Low flow velocity (close state) results from a trapped ion at the entrance (inset scheme) and high flow velocity (open state). (*d*) Flow velocity (orange squares) and ionic flux (green spheres) as functions of pressure gradient. Simulation results agree with non-equilibrium theory (solid lines). The dashed line denotes flow velocity derived from Sampson's solution.

physical origin for limiting the selectivity-permeability trade-off in RO. Our work offers a molecular-level understanding and statistical framework for RO that identifies ion trapping at membrane interfaces as the fundamental performance-limiting mechanism in RO. This phenomenon can be extended to much broader fields, for instance, electro-osmosis and thermo-osmosis in Ångström-scale systems when ions penetrate into the channel under generic forces.

## 2. Methods

We performed NEMD simulations using Large-scale Atomic/Molecular Massively Parallel Simulator (Thompson *et al.* 2022) to study water and ionic transport through a 0.33 nm radius, 10 nm long Ångström tube clamped by two 3.1 × 3.1 nm Face-Centered Cubic (FCC) membranes with 4.48 Å lattice parameter (figure 1*a*). The left box contained 0.3 M NaCl, and the right contained pure water, using TIP3P water molecules and an optimised ion model for NaCl (Jorgensen *et al.* 1983; Joung & Cheatham 2008). We employed Lorentz–Berthelot mixing rules to calculate the heteronuclear LJ interaction parameters with solid atoms $\sigma_{ss} = 3.37$ Å, $\epsilon_{ss} = 0.0361$ eV. The low frictional wall enables high water permeability in system. Water molecules could fill in the nanotube within 1 ns after thermal equilibrated at 289 K using a Nosé–Hoover thermostat at 1 atm by applying forces at the outermost wall. We computed long-range Coulomb interactions using the particle-particle particle-mesh (PPPM) algorithm with periodic boundary conditions in



https://doi.org/10.1017/jfm.2025.10961 Published online by Cambridge University Press

all directions. In our NEMD simulations, the pressure $P_1$ and $P_2$ were applied to the left and right membrane, the pressure drop $\Delta p = P_1 - P_2$ increased from 4000 to 42 000 bar along the channel's longitudinal (z) direction by increasing force on the leftmost membrane for hydrodynamic flows. We conducted three independent simulations for each $\Delta p$ value, each lasting over 5 ns, to obtain water velocity and ionic fluxes. The error bars of velocity and fluxes were the standard deviation calculated from those three independent simulations. To minimise salt concentration changes in the left reservoir, data were collected only when its concentration increased by less than 10 %. In all simulations, the outermost wall was fixed in the radial plane but allowed to move in the $z$-direction. The rest of the wall and tube vibrated around the equilibrium position, with a harmonic spring (spring constant $K = 25\,\text{ev}\,\text{Å}^{-2}$) attached to each solid particle. Here we use umbrella sampling by applying biasing potentials along the axial coordinate of the nanotube, enabling us to characterise the potential of mean force (PMF) for the free energy barrier in our nanotube system. The sampling coordinate of the umbrella sampling calculations ranged between $z = -6$Å and $z = 3$ Å. The $Na^+$ and $Cl^-$ ions were translocated along the sampling coordination, respectively, to systematically replace individual water molecules, resulting in 12 distinct sampling windows per ion species. In each window, a harmonic bias potential was applied to ensure sufficient overlap with adjacent windows. Molecular dynamics simulations of 2 ns were performed per window, and the final 1.5 ns of each trajectory was used for analysis. The unbiased PMF was reconstructed using the weighted histogram analysis method (WHAM). The theoretical foundations of umbrella sampling are detailed in Kästner (2011).

## 3. Results

We first measured the averaged PMF for $Na^+$ and $Cl^-$ ions along the $z$-direction by using umbrella sampling (figure 1*b*). The PMF increases significantly at the nanotube vicinity caused by the dielectric and dehydration energy barrier (Esfandiar *et al.* 2017; Zhou & Xu 2020; Zhan *et al.* 2020), as the basis for ion rejection. For later calculations, we numerically fitted the PMF in the form of a logistic function $\phi_B = \phi_0/(1 + e^{-z/\delta})$. The energy barrier $\phi_0$ can be estimated as $\phi_0 = \phi_{dh} + \phi_{de}$, as the summation of $\phi_{dh}$ arising from ion dehydration (Esfandiar *et al.* 2017) and dielectric repulsion $\phi_{de}$ due to the water permittivity contrast from bulk to the confinement, and the $\delta$ determined profile of the energy barrier at the nanotube entrance that we can fit from PMF in simulation.

Figure 1(*c*) shows the averaged flow velocity $v_w(t)$ inside the nanotube as time passed, with a mean velocity every 10 ps.

We observed that the flow velocity alternates between high (light cyan background) values as an 'open' state and low values as a 'close' state. The 'close' state is attributed to a trapped ion near the nanotube entrance (see inset in figure 1*c*) that is also noted in previous work (Su *et al.* 2019; Li *et al.* 2022). The trapped ion, either $Na^+$ or $Cl^-$, increases the system friction, thereby reducing the flow velocity. The flow velocity increases again once the trapped ion leaves the entrance. The trapping behaviour of ions at the tube entrance is governed by the joint actions of the energy barrier and the hydrodynamic forces, where the hydrodynamic forces on hydrated ions push the ions toward the nanotube, against the nanotube energy barrier.

The time-averaged ion flux, $j_{ion}(t) = (1/t)\sum_{i=1}^{n} n_i(t)$ shown as green dots in figure 1(*d*), remains negligible at the pressure gradient ($\nabla P$) below 2000 bar nm$^{-1}$, where $n$ is the number of ions transported through the nanotube within a time interval $t$. However, ion flux increases dramatically with $\nabla P$, consistent with the trend of previous experimental



https://doi.org/10.1017/jfm.2025.10961 Published online by Cambridge University Press

observations (Zhang *et al.* 2020; Biesheuvel *et al.* 2023; Wang *et al.* 2021, 2023) but contradicts the prediction of the SD model. The deviation in critical pressure for ion flux emergence is due to the channel size, friction coefficient and other detailed parameters. We will discuss the size effects in later texts.

The averaged water flow velocity is calculated as $v_w = \langle (1/n) \sum_{i=1}^{n} v_i(t) \rangle$, where $n$ is the number of water molecules in the nanotube, and $v_i(t)$ is the stream velocity of water molecules measured between 0.2 nm downstream of the tube entrance and 0.2 nm upstream of the exit to minimise the effect of entrance/exit on the velocity. The velocity of water molecules in the first 100 ps was not included to eliminate the transient effects of undeveloped flow. The flow velocity exhibits a more complex behaviour than the ionic flux. For $\nabla P < 1000\,\mathrm{bar\,nm^{-1}}$, $v_w$ aligns with Sampson's solution (dashed line in figure 1*d*). However, as $\nabla P$ increases, $v_w$ unexpectedly decreases, representing an NDFR effect. When $\nabla P$ is over $2000\,\mathrm{bar\,nm^{-1}}$, $v_w$ rapidly increases with $\nabla P$ again meanwhile ionic flux emerges. The pressure gradient ($\nabla P$) applied in NEMD simulations is orders of magnitude larger than in experiments, as it must drive sufficient water transport within a few nanoseconds despite thermal noise. Nevertheless, ionic blockade at the pore entrance persists even in larger pores under much lower pressures.

## 4. Theoretical analysis

### 4.1. *Theoretical analysis for ionic flux*

We employed the 1D Fokker–Planck equation (FPE) as a non-equilibrium statistic theory framework to capture the ion permeation along the $z$-direction:

$$\frac{\partial W}{\partial t} = D\left[\frac{\partial}{\partial z}\left(\frac{\partial \phi_z}{k_B T \partial z} W\right) + \frac{\partial^2 W}{\partial z^2}\right] \tag{4.1}$$

where $W(z,t)$, $D$, $z$, $k_B T$ are probability density of ions, diffusion coefficient of ions, displacement in the $z$-direction. $k_B$ is Boltzmann constant and $T$ is temperature, respectively. Here we consider $Na^+$ and $Cl^-$ as identical ions, although the slightly different hydrated radius may cause little deviation. The potential field $\phi_z = (\phi_B - \Delta\mu) - f_h z$ includes the energy barrier $\phi_B$, chemical potential $\Delta\mu$, and work done by hydrodynamic friction on a single ion $f_h z$ with Stokes' drag force $f_h = 6\pi\eta\sigma_{ion} v_{w,o}$, where $\eta$, $\sigma_{ion}$, $v_{w,o}$ are the water viscosity, ion's hydrated radius and flow velocity at nanotube entrance derived from Sampson's solution. Here we use the bulk water viscosity, since the trapped ion primarily remains in the bulk water, as shown in figure 8 in Appendix C. The Sampson solution in pure water (dashed line in figure 1*d*) is validated by the agreement with the measured water velocity in the absence of ion trapping ($v_{w,o}$), and the flow velocity at $\nabla P < 1000\,\mathrm{bar\,nm^{-1}}$ where the probability of ion trapping is small. Here we take $Na^+$ and $Cl^-$ as identical particles with an averaged hydrated radius of 1.7 Åin calculations. In our system, the chemical potential $\Delta\mu = \mu_L - \overline{\mu} = R_a T \ln(C_L/\bar{C})$ is much lower than the energy barrier $\phi_B$ and no ion permeation is observed without applying pressure,where $R_a$,$T$,$C_L$, $\bar{C}$ are gas constant, temperature and concentration of the left reservoir and the system. Here $\mu_L$, $\overline{\mu}$ are chemical potentials of the left reservoir and the system, respectively.

We could numerically derive the absorbing boundary ($d'$) by setting $(d\phi_z/d'z)|_{d'} = 0$. Thus, the first mean passage time (FMPT) for an ion penetrating the energy barrier and entering the nanotube can be derived as $\tau_{t,z}$:

$$\tau_{t,z} = \frac{1}{D}\int_0^{d'} \mathrm{e}^{-\frac{\phi_z}{k_B T}}\,\mathrm{d}z \int_z^{d'} \mathrm{e}^{\frac{\phi_{z'}}{k_B T}}\,\mathrm{d}z'. \tag{4.2}$$



https://doi.org/10.1017/jfm.2025.10961 Published online by Cambridge University Press

Here we consider a unit cell of water containing a pair of $Na^+$, $Cl^-$ ions within a volume of $(N_A C)^{-1}$, and use it to estimate the probability that there is an ion thermodynamically moving in front of the nanotube, where $N_A$ and $C$ are Avogadro's number and salt concentration. The critical time of flow in the absence of ion trapping is given by $\tau_o = (\pi N_A C v_{w,o} R^2)^{-1}$, where the flow velocity $v_{w,o}$ in the nanotube is derived from Sampson's solution $v_{w,o} = \Delta p/\lambda_{nt}$ with nanotube friction $\lambda_{nt} = (3\pi\eta/R) + (2L\lambda_w/R)$ accounting for the entrance (first term) and nanotube wall (second term), respectively. This $\lambda_w$ is the friction coefficient of the nanotube wall that we measured from Green–Kubo relations. $R$ and $L$ are the radius of tube and length of tube respectively. Thus, the ionic flux correlates with the FMPT of ions trapped at the entrance, $\tau_{tz}$, and the critical time of water in the unit cell flowing through the nanotube without ion trapping, $\tau_o$:

$$j_{ion} = \frac{2}{\tau_o + \tau_{t,z}}. \tag{4.3}$$

Our theoretical results (solid green line in figure 1*d*) agree well with the ionic fluxes from the MD simulation (green dots). Here we define a dimensionless factor $\mathcal{P}_\mathcal{Z} \equiv \tau_o/(\tau_o + \tau_{t,z})$ to characterise the suppression of ionic flux by the energy barrier, hence ionic fluxes can be written as $j_{ion} = \mathcal{P}_\mathcal{Z} j_{max}$. The flux reaches its maximum when $\mathcal{P}_\mathcal{Z}$ approaching 1 (i.e. vanishing barrier), where $j_{max} = 2\pi N_A C v_{w,o} R^2$ is the maximum ionic flux in the absence of an energy barrier. At low $\nabla P$, $\mathcal{P}_\mathcal{Z} \ll 1$, the hydrodynamic force is insufficient to overcome the energy barrier $\phi_B$, resulting in negligible ionic fluxes. As $\nabla P$ increases, ion permeation increases significantly due to enhanced hydrodynamic force on the trapped ion.

### 4.2. *Theoretical analysis for water velocity*

Now we consider the flow velocity. We observe a high flow velocity $v_o$ in the absence of ion trapping and a low velocity state $v_c$ when trapped ions give additional friction in our system in figure 1(*c*). Simulations show that trapped ions can turn back to the reservoir instead of penetrating through, thus reopening the nanotube for water permeation. Hence, we incorporate the axial symmetric radial escape rate $\tau_r^{-1}$ of the trapped ion. Trapping occurs due to hydrodynamic friction with radial shear stress, with maximum flow velocity along the axis (figure 2*a*) (Heiranian, Taqieddin & Aluru 2020). According to Langer theory (Langer 1969; Berezhkovskii, Pollak & Zitserman 1992; Collins *et al.* 2014), the escape rate is determined by the saddle-point route, where particles are most likely to escape. In our system, ions experience the smallest hydrodynamic forces at the nanotube's outer membrane boundary. Thus, we calculate the radial escape rate of a trapped ion shown as the orange dashed line in figure 2(*a*). Hence, the bidirectional escape rate $\tau_t^{-1}$ for the trapped ion, schematically shown in figure 2(*b*), is the sum of both radial and axis directions:

$$\tau_t^{-1} = \tau_{t,z}^{-1} + \tau_{t,r}^{-1}. \tag{4.4}$$

Thus, we need to consider the radial escape rate. By taking the hydrodynamic friction energy of the trapped ion to an ordinary FPE:

$$\frac{\partial W}{\partial t} = D\left[\frac{\partial}{\partial r}\left(\frac{\partial \phi_r}{k_B T \partial r} W\right) + \frac{\partial^2 W}{\partial r^2}\right], \tag{4.5}$$

where $W(r, t)$ and $r$ are the probability density of the ions in the radial direction and displacement in the $r$-direction, respectively. Here $\phi_r = f_z(r) \times r$ represents the work done by hydrodynamic friction on the trapped ion. We could calculate the FMPT $\tau_{t,r}$



https://doi.org/10.1017/jfm.2025.10961 Published online by Cambridge University Press

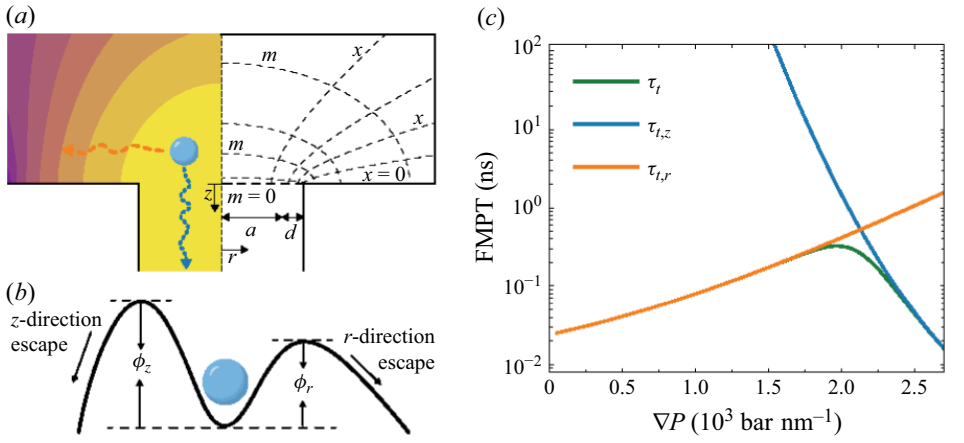



Figure 2. (*a*) The flow velocity distribution at the entrance of the nanotube is derived by Heiranian *et al.* (2020), where colour indicates the velocity from high (yellow) to low (purple). (*b*) Scheme of trapped ion (blue in figure 2*a*) and bidirectional escape from radial and axial directions of nanotube. (*c*) The FMPT as a function of pressure gradient.

in the radial direction by defining the friction force on the trapped ion following Stokes' laws as $f_z(r) = f_h g(r)$, where the first term is $f_h = 6\pi\eta\sigma_{ion}$. Here $\eta$ is the water viscosity and $\sigma_{ion}$ is the hydrated radius of ions. The function $g(r)$ represents the radial velocity distribution at the nanotube entrance, calculated from the stream function $\psi(r, z)$ in cylindrical coordinates. As shown in figure 2(*a*), $\psi(r, z)$ was calculated from spheroidal coordinates ($x$,$m$) according to Heiranian *et al.* (2020), and the details are in Appendix A. Thus the FMPT $\tau_{t,r}$ for a specific angle $\theta$ is calculated as

$$\tau_{t,r,\theta} = \frac{1}{2\pi D}\int_0^R \mathrm{e}^{-(\phi_r/k_BT)}\mathrm{d}r \int_r^R \mathrm{e}^{(\phi_{r'}/k_BT)}\mathrm{d}r'. \tag{4.6}$$

Considering the axisymmetric radial escape from the hydrodynamic trap, we have

$$\tau_{t,r} = (2\pi)^{-1}\tau_{t,r,\theta}. \tag{4.7}$$

The calculated FMPT of the trapped ion is shown in figure 2(*c*). The FMPT $\tau_{t,r}$ increases with $\nabla P$ due to enhanced hydrodynamic friction on trapped ions, which slows radial escape. In contrast, $\tau_{t,z}$ decreases as hydrodynamic forces facilitate ion permeation. At low $\nabla P$, $\tau_t$ increases, dominated by $\tau_{t,r}$. As $\nabla P$ rises, $\tau_t$ peaks when $\tau_{t,z} \approx \tau_{t,r}$, corresponding to equal ion escape rates in the radial and axial directions, leading to maximum friction at the entrance and the observed NDFR phenomenon (figure 1*d*). Beyond this point, $\tau_t$ decreases and converges with $\tau_{t,z}$. These results suggest that at low $\nabla P$, trapped ions escape radially due to thermal fluctuations, while higher $\nabla P$ enhances ion permeation, reducing the ion trapping time $\tau_t$.

We derive the flow velocity from the velocity in the open state ($v_{w,o}$) and close state ($v_{w,c}$), along with their probabilities determined by FMPTs:

$$v_w = \mathcal{P}_\mathcal{S} \cdot v_{w,o} + (1 - \mathcal{P}_\mathcal{S}) \cdot v_{w,c}. \tag{4.8}$$

The flow velocity with a trapped ion (close state) is $v_{w,c} = \Delta p/(\lambda_{nt} + \lambda_{ion})$, where the additional friction term $\lambda_{ion} = 6\eta\sigma_{ion}R^{-2}$ arises from Stokes' drag on the trapped ion. The factor $\mathcal{P}_\mathcal{S} \equiv \tau_o/(\tau_t + \tau_o)$ represents the probability of the open state, while



https://doi.org/10.1017/jfm.2025.10961 Published online by Cambridge University Press

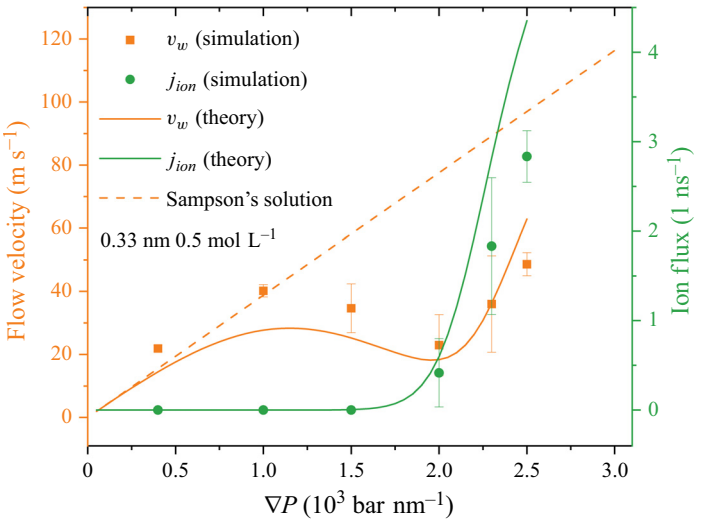



Figure 3. The flow velocity (orange) and ionic fluxes (green) through a 0.33 nm radius nanotube in 0.5 M electrolyte solution. The simulation results (scatters) also demonstrated the NDFR phenomenon in the nanotube, which aligns well with theoretical calculations.

$1-\mathcal{P}_S$ corresponds to the close state probability, where $\tau_t$ is the bidirectional escape time determined by (4.2), and $\tau_o$ is the critical time of flow in the absence of ion trapping.

Considering the coupling between chemical potential and pressure gradient, we have the ion flux ($j_{ion}$) and water flux ($j_w = \rho_z v_w$) in Onsager matrix (Mason & Lonsdale 1990; Monet *et al.* 2023), where $\rho_z = N/L$ is the linear density of water molecules along the nanotube axis with total water molecules $N$ and nanotube length $L$:

$$\begin{pmatrix} j_{ion} \\ j_w \end{pmatrix} = \begin{pmatrix} m_{11} & m_{12} \\ m_{21} & m_{22} \end{pmatrix} \begin{pmatrix} \Delta\mu \\ \Delta P \end{pmatrix}, \tag{4.9}$$

where $m_{11}$, $m_{12}$, $m_{21}$ and $m_{22}$ are diffusive diffusion, excess flux under pressure, diffusio-osmotic flow coefficient and water permeability under pressure, respectively. To derive the permeabilities of water and ions, we take the chemical potential $\Delta\mu = \mu_L - \overline{\mu} = R_a T \ln(C_L/\bar{C})$ in the matrix. Thus, we have the ion permeation $B = (m_{11}/R_a TA) + m_{12}$ which can be simplified to $B \simeq m_{12} = (2\pi N_A C R^2/\lambda_{nt})\mathcal{P}_{\mathcal{Z}}$, and water permeation becomes $A = (m_{21}/R_a TA) + m_{22}$ that can be simplified to $A \simeq m_{22} = (\rho_z \mathcal{P}_S/\lambda_{nt}) + (\rho_z(1-\mathcal{P}_S)/(\lambda_{nt}+\lambda_{ion}))$, since the chemical potential is insufficient to drive transport through the nanotube in our case.

To validate our statistical theories, we approved our theory for a 0.33 nm radius nanotube in 0.5 M NaCl solution – a higher concentration than that in figure 1(*d*), which is a typical NaCl concentration in seawater. The results shown in figure 3 indicate our theory could also explain the influence of salt concentration under dilute conditions according to (4.3), (4.8) and $\tau_o$. The increased salt concentration reduces $\tau_o$, thus decreasing the flow velocity and increasing the ion permeability (compared with the solid line in figures 1*d* and 3), in agreement with the tendency in experimental observations (Wang *et al.* 2021). In addition, our theory can also capture the size effect on the flow velocity and ionic flux since the theoretical prediction agrees well with the result from the simulation for a 0.29 nm radius



https://doi.org/10.1017/jfm.2025.10961 Published online by Cambridge University Press

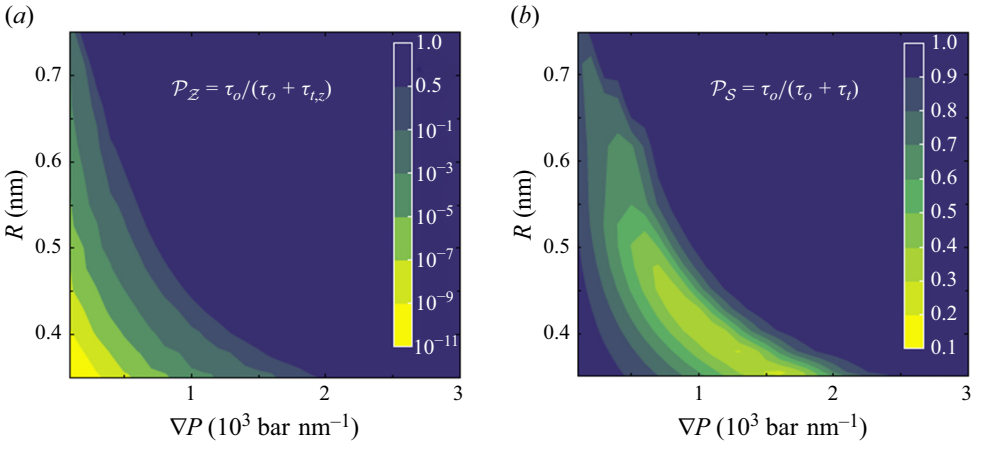



Figure 4. Phase diagram of permeabilities for ions (*a*) and water (*b*) as functions of pressure gradient and channel radius. Both phase diagrams share the same *y*-axis.

nanotube with 0.3 M shown in figure 9 in Appendix D. However, we neglected the ion–ion interactions in the FPE for ions penetrating the nanotube under dilute conditions, but such interactions may become significant in highly concentrated solutions or ionic liquids where ion pairs are formed in the solution.

As the energy barrier of nanotubes scales inversely with radius, $\phi_0 \propto R^{-1}$, according to (Parsegian 1969; Richards *et al.* 2012*a*,*b*; Fumagalli *et al.* 2018), we can further explore the size effects in RO. By replacing $\phi_B$ with the corresponding value for nanotubes at different sizes to our previous theories, we derived ion and water permeabilities as functions of $\nabla P$ and $R$. Our results indicate a monotonic increase in ion permeability ($B \propto \mathcal{P}_\mathcal{Z}$) with both parameters, ranging from low (yellow) to high (blue) in figure 4(*a*), as $\tau_{t,z}$ decreases with increasing $\nabla P$ or decreasing $R$. When $\tau_o \ll \tau_{t,z}$, $B$ increases exponentially with $\nabla P$, approaching 1 as $\tau_o \gg \tau_{t,z}$ and the energy barrier becomes negligible. The water permeability $A$ in figure 4(*b*) shows a distinct valley (yellow), indicating the NDFR regime. We identify a threshold radius of $R < 0.7$ nm for observable NDFR in our simulation, with the critical $\nabla P$ shifting to lower values as $R$ increases. The NDFR behaviour vanishes when $\lambda_{ion}$ becomes negligible or when ion trapping probability is significantly reduced ($\mathcal{P}_\mathcal{Z} \approx 1$).

With the water permeability $A$ and ion permeability $B$, we have the selectivity between water and ions as $\alpha = A/B$. To demonstrate the impact of NDFR on RO, we calculate the selectivity-water flux ($\alpha$ vs $j_w$) curve for a 0.33 nm radius nanotube (figure 5). Without NDFR effects, selectivity decreases as water flux increases, reflecting the trade-off limit. Incorporating NDFR introduces a concave region in the trade-off curve, indicating unattainable selectivity-water flux combinations. These NDFR effects diminish as the nanotube radius increases, weakening the hydrodynamic trap for ions.

To demonstrate the NDFR is preserved in a more realistic channel, we performed molecular dynamics simulations on a $m(10, 0)$ carbon nanotube (CNT) using the settings detailed in Appendix B, with corresponding results in figure 7. Experimentally observing the NDFR effect in a single Ångström channel remains challenging due to intrinsically low flow rates, even in low-friction systems. However, unconventional approaches may overcome this limitation. For instance, the nanojet method (Secchi *et al.* 2016) can directly

https://doi.org/10.1017/jfm.2025.10961 Published online by Cambridge University Press

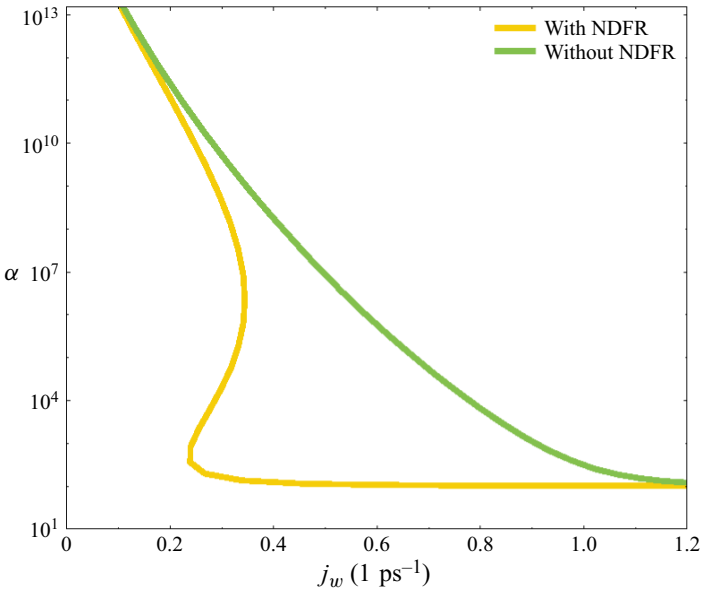



Figure 5. Selectivity-water flux trade-off in a single nanotube with radius of 0.33 nm. The NDFR effect strongly reduces the performance of RO in a single nanotube.

visualise nanoscale flows, and fluorescence correlation spectroscopy (Li *et al.* 2024*b*) could provide alternative means to characterise such low flow rates.

Interestingly, the NDFR phenomenon has not been reported in RO experiments, even if ion trapping could happen in practice. To investigate this discrepancy, we consider a membrane composed of parallel channels with a certain size distribution, as reported in previous experimental systems (Otero *et al.* 2008; Wang *et al.* 2024). The pore size distribution is shown in the inset of figure 6. We calculate the selectivity of a membrane as $\alpha_m = \sum p_i \alpha_i$ where $p_i$ and $\alpha_i$ are the probability at a specific channel size and the selectivity we derived in the corresponding channel size, according to previous text. The water flux is simply calculated by the summation of all channels $j_{m,w} = \sum j_{i,w}$ where $j_{i,w}$ is the water flux from an individual channel.

Our results in figure 6 demonstrate that NDFR vanishes in such a membrane due to statistical averaging in a certain wide channel size distribution. Since the threshold of the NDFR phenomenon is strongly correlated to the channel size, the overall effect becomes suppressed when averaging across many pores with varying diameters. This statistical averaging likely masks NDFR in experimental measurements. Here, we did not account for hydrodynamic interactions between densely packed parallel pores, which may enhance water flow permeation according to previous studies (Jensen, Valente & Stone 2014). Our system behaves as a membrane with sparsely distributed pores, enabling us to evaluate its performance from the response of a single channel.

Nonetheless, ion trapping at the channel entrance still leads to a substantial reduction in the selectivity-permeability trade-off, even in the absence of observable NDFR for a membrane. This ion trapping arises from dielectric exclusion as well as ion dehydration and manifests as a size-dependent energy barrier, as previously described by the FMPT framework. Therefore, ion trapping remains an intrinsic and dominant constraint on RO performance, regardless of optimal pore size or low-friction channel conditions.



https://doi.org/10.1017/jfm.2025.10961 Published online by Cambridge University Press

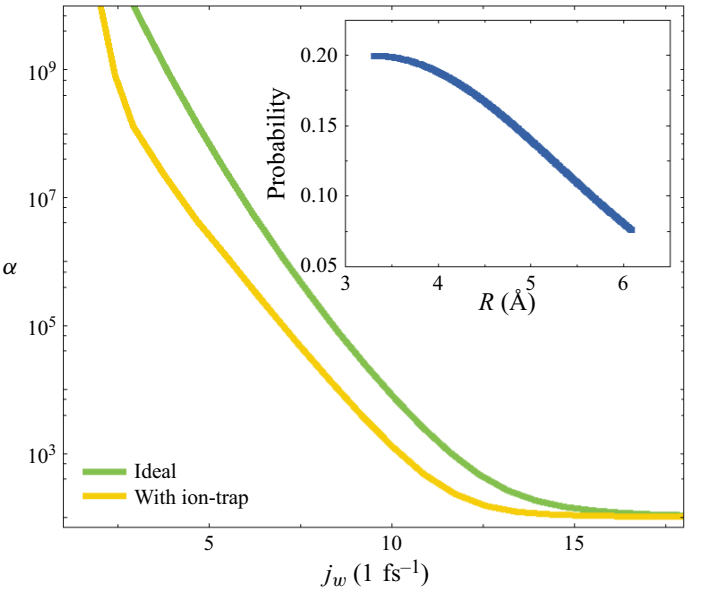



Figure 6. The NDFR phenomenon vanishes in parallel embedded nanotube membranes due to statistical averaging over a sufficiently broad channel size distribution (inset), which explains its absence in experimental observations. However, ion trapping significantly reduces the selectivity-permeability trade-off, becoming a predominant limiting factor in RO. The inset shows the probability distribution of the parallel channel sizes.

## 5. Conclusions

In summary, we investigate the ion and water permeation through a single Ångström channel by pressure-driven flow, using a non-equilibrium statistical framework supported by all atom MD simulations. Our theory explains ion rejection at low pressure gradients due to a dielectric and dehydration energy barrier and ion permeation as pressure increases. Notably, we discovered an NDFR phenomenon, driven by ion trapping at the channel entrance, giving additional friction to the system. Our bidirectional escape model captures the NDFR effect by FMPT and provides quantitative descriptions for ion and water permeation as functions of channel radius and pressure gradient. Furthermore, we reveal a selectivity-water flux trade-off, which deviates from the classical SD model, with a statistical mechanics framework for RO. Although not all the effects like concentrations were explored here, our work provides statistical mechanics insights into RO, explaining previous observations and predicting new phenomena like NDFR.

**Acknowledgements.** The authors thank the anonymous referees for their helpful comments that improved the quality of the manuscript, M. Sun for the support of figure drawing, and S. Luan for the help of manuscript preparation.

**Funding.** This work was supported by the National Natural Science Foundation of China (grant nos 12388101 and 12241201).

**Declarations of interests.** The authors report no conflict of interest.

## Appendix A. Calculation of stream function $\psi(r, z)$

Here, we derived $\psi(r, z)$ by using the stream function $\psi$ in spheroidal coordinates $(x,m)$ according to Heiranian *et al.* (2020):



https://doi.org/10.1017/jfm.2025.10961 Published online by Cambridge University Press

$$\psi = \begin{cases} \dfrac{1}{2\pi} Q x^3 & \text{for } b < x \leqslant 1, \\ \dfrac{1}{2\pi} Q x^3 \left( \dfrac{2x}{b} - \dfrac{x^2}{b^2} \right) & \text{for } 0 < x \leqslant b, \end{cases} \tag{A1}$$

where $Q = v_{w,o} \pi R^2$ is the flow rate, $R$ is the nanotube radius and $b$ corresponds to $d$ as in (A2) and (A3) in cylindrical-polar coordinates.

Following Heiranian *et al.* (2020), we take coordinate transformation from the confocal hyperbolas and ellipses oblate spheroidal coordinates, denoted by $x$ and $m$, respectively, to the radial distance from the centre of the orifice (denoted by $r$) and distance from the nanotube entrance in cylindrical coordinates by using (A2) and (A3). We presented the stream function $\psi$ in spheroidal coordinates at the nanotube entrance in both oblate spheroidal coordinates and cylindrical coordinates in figure 2(*a*):

$$r^2 = \left[ m^2 + (a+d)^2 \right] \left( 1 - x^2 \right), \tag{A2}$$

$$z^2 = m^2 x^2. \tag{A3}$$

By substituting (A2) and (A3) into (A1), we obtain the stream function $\psi(r, z)$ in cylindrical coordinates. The velocity distribution $g(r)$ is then derived from the partial derivative of the stream function as $(1/r)(\partial \psi(r, z)/\partial z) = g(r)$. We define the absorbing boundary at the nanotube radius $r = R$, beyond which ions can no longer be trapped. The hydrodynamic friction energy well is given by $\phi_r = f_h g(r) r$.

## Appendix B. NDFR effect in CNT

Here we performed additional MD simulations to validate this NDFR phenomena in carbon nanotube. Figure 7 shows velocity (orange squares) and ionic flux (green spheres) as a function of the pressure gradient in an $m(10, 0)$ carbon nanotube (CNT). Following the configuration as in the main text including the ion and water model, we conducted NEMD simulations to examine water and ionic transport through an $m(10, 0)$ carbon nanotube with 10 nm length graphene walls used as membrane to drive the flows. Following settings in Algara-Siller *et al.* (2015); Li *et al.* (2024*a*), the atoms in graphene walls and carbon nanotubes are modelled by LJ potentials with parameter atoms with $\sigma_{cc} = 3.4$ Å, $\epsilon_{cc} = 0.00371$ eV. The water and carbon interactions are also modelled by LJ potentials with parameter $\sigma_{co} = 3.276$ Å, $\epsilon_{co} = 0.00494$ eV (Cornell *et al.* 1995) and other heteronuclear LJ interactions were determined by Lorentz–Berthelot mixing rules. Following thermal equilibration at 289 K under a Nosé–Hoover thermostat and 1 atm pressure, the nanotube was filled with water molecules within 1 ns. Long-range Coulombic interactions were computed using the PPPM algorithm, with periodic boundary conditions applied in all directions. In NEMD simulations, hydrodynamic flow was induced along the longitudinal ($z$) axis by imposing a pressure differential $\Delta p = P_1 - P_2$ across the nanotube.

Similar as in the generic LJ systems, we also observed the NDFR phenomena of water flow and pressure-dependent ionic flux in CNT. The statistically counted ion and water fluxes were shown as yellow and green dots in figure 7. The ionic fluxes show nonlinear increases as the pressure gradient $\Delta p$, while the water fluxes at $10^3$ bar nm$^{-1}$ are apparently higher than the value at $1.5 \times 10^3$ bar nm$^{-1}$ representing a NDFR.

## Appendix C. Probability distribution of trapped ion

As shown in figure 8, the trapped ions are typically in front of the nanotube, not inside of the nanotube, that justifies using bulk viscosity and Stokes' force in the main text.



https://doi.org/10.1017/jfm.2025.10961 Published online by Cambridge University Press

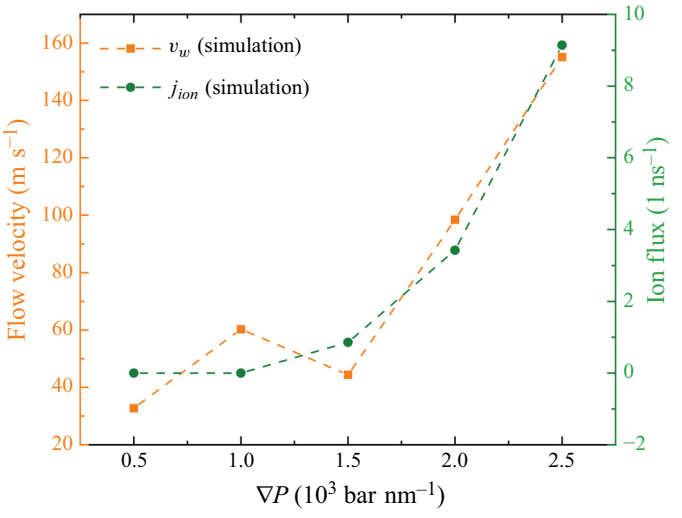



Figure 7. The water velocity and ionic flux as a function of pressure gradient in m10 CNT. The dashed lines are used as guidance.

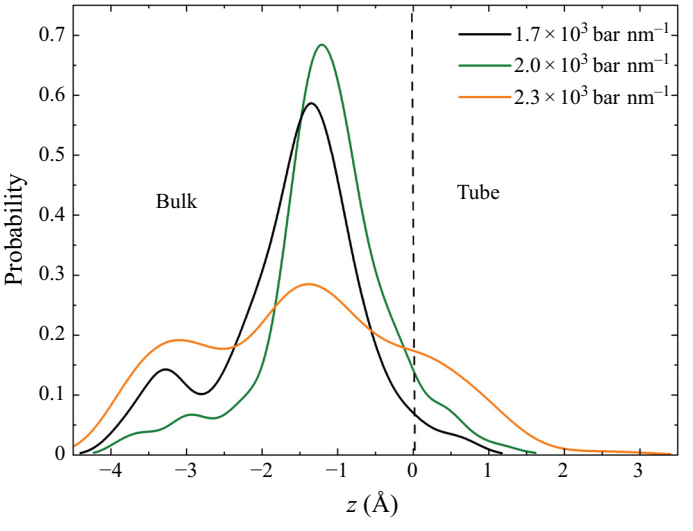



Figure 8. The distribution probability of trapped ions under three different pressure gradients. The dashed line indicates the entrance of the nanotube.

## Appendix D. MD simulation results in 0.29 nm radius nanotube

Figure 9 shows velocity (orange squares) and ionic flux (green spheres) as a function of the pressure gradient from the molecular dynamics simulation for an LJ tube with 0.29 nm radius. The orange solid line and green solid line calculated from the statistic theory presented in the main text agree with the simulation data (dots). Here we followed all settings as § 2. We conducted NEMD simulations to examine water and ionic transport through a single-Ångström-diameter nanotube with a radius of 0.29 nm and a length of 10 nm. The system was made from an FCC solid with a lattice parameter of 4.1 Å, while the ion and water model is the same as the one inthe main text. The LJ parameters for solid



https://doi.org/10.1017/jfm.2025.10961 Published online by Cambridge University Press

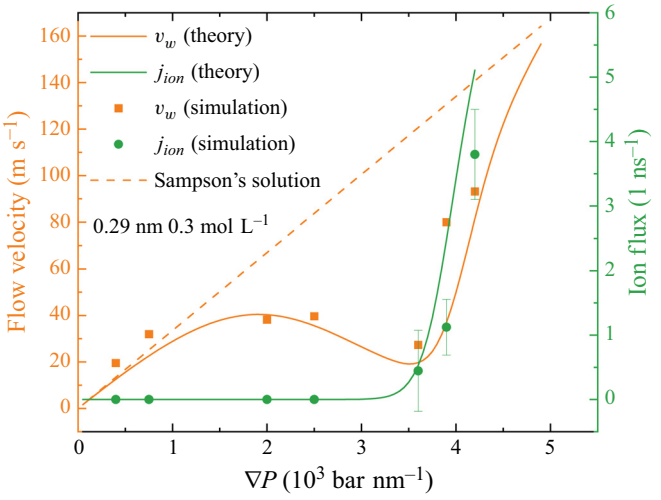



Figure 9. The simulation data (scattered points) with theoretical predictions (solid lines) across different pressure gradients. The simulation data closely align with the theoretical models. Water velocity (orange squares) matches the ion-free Sampson solution at both low and high pressure gradients, demonstrating an NDFR effect.

atoms defined as $\sigma_{ss} = 3.37$ Å, $\epsilon_{ss} = 0.0251$ eV were used with Lorentz–Berthelot mixing rules for heteronuclear LJ interaction, hence the water molecules can fill the nanotube within 1 ns after thermal equilibration at 289 K under a Nosé–Hoover thermostat and 1 atm pressure. Long-range Coulomb interactions were calculated using the PPPM algorithm, and periodic boundary conditions were applied in all directions. In the NEMD simulations, the pressure drop $\Delta p = P_1 - P_2$ across the nanotube was varied from 4000 to 42 000 bar along the longitudinal $z$-direction by increasing the force on the leftmost membrane to drive hydrodynamic flow. For each $\Delta p$ value, three independent simulations were performed to determine water velocities and ionic fluxes. Throughout the simulations, the outermost walls were fixed in the radial direction, but enabled to move along the $z$-direction. Meanwhile, the remaining walls and the nanotube vibrated around their equilibrium positions, restrained by harmonic springs with a spring constant of $K = 25$ ev/Å$^2$.

## References


Algara-Siller, G., Lehtinen, O., Wang, F.C., Nair, R.R., Kaiser, U., Wu, H.A., Geim, A.K. & Grigorieva, I.V. 2015 Square ice in graphene nanocapillaries. *Nature* **519** (7544), 443–445.

Aluru, N.R. *et al.* 2023 Fluids and electrolytes under confinement in single-digit nanopores. *Chem. Rev.* **123** (6), 2737–2831.

Baldock, H. & Huang, D.M. 2024 Scaling laws for concentration-gradient-driven electrolyte transport through a 2d membrane. arXiv preprint arXiv: 2412.03781.

Berezhkovskii, A.M., Pollak, E. & Zitserman, V.Y. 1992 Activated rate processes: generalization of the kramers–grote–hynes and langer theories. *J. Chem. Phys.* **97** (4), 2422–2437.

Biesheuvel, P.M., Dykstra, J.E., Porada, S. & Elimelech, M. 2022 New parametrization method for salt permeability of reverse osmosis desalination membranes. *J. Memb. Sci. Lett.* **2** (1), 100010.

Biesheuvel, P.M., Rutten, S.B., Ryzhkov, I.I., Porada, S. & Elimelech, M. 2023 Theory for salt transport in charged reverse osmosis membranes: novel analytical equations for desalination performance and experimental validation. *Desalination* **557**, 116580.

Bocquet, L. 2020 Nanofluidics coming of age. *Nat. Mater.* **19** (3), 254–256.

Collins, P., Kramer, Z.C., Carpenter, B.K., Ezra, G.S. & Wiggins, S. 2014 Nonstatistical dynamics on the caldera. *J. Chem. Phys.* **141** (3), 034111.




https://doi.org/10.1017/jfm.2025.10961 Published online by Cambridge University Press

COMTET, J., RAYABHARAM, A., GLUSHKOV, E., ZHANG, M., AVSAR, A., WATANABE, K., TANIGUCHI, T., ALURU, N.R. & RADENOVIC, A. 2021 Anomalous interfacial dynamics of single proton charges in binary aqueous solutions. *Sci. Adv.* **7** (40), eabg8568.

CORNELL, W.D., CIEPLAK, P., BAYLY, C.I., GOULD, I.R., MERZ, K.M., FERGUSON, D.M., SPELLMEYER, D.C., FOX, T., CALDWELL, J.W. & KOLLMAN, P.A. 1995 A second generation force field for the simulation of proteins, nucleic acids, and organic molecules. *J. Am. Chem. Soc.* **117** (19), 5179–5197.

CULP, T.E. *et al.* 2021 Nanoscale control of internal inhomogeneity enhances water transport in desalination membranes. *Science* **371** (6524), 72–75.

DI VINCENZO, M., TIRAFERRI, A., MUSTEATA, V.-E., CHISCA, S., DELEANU, M., RICCERI, F., COT, D., NUNES, S.P. & BARBOIU, M. 2021 Tunable membranes incorporating artificial water channels for high-performance brackish/low-salinity water reverse osmosis desalination. *Proc. Natl Acad. Sci.* **118** (37), e2022200118.

DUCHANOIS, R.M., HEIRANIAN, M., YANG, J., PORTER, C.J., LI, Q., ZHANG, X., VERDUZCO, R. & ELIMELECH, M. 2022 Designing polymeric membranes with coordination chemistry for high-precision ion separations. *Sci. Adv.* **8** (9), eabm9436.

ESFANDIAR, A., RADHA, B., WANG, F.C., YANG, Q., HU, S., GARAJ, S., NAIR, R.R., GEIM, A.K. & GOPINADHAN, K. 2017 Size effect in ion transport through angstrom-scale slits. *Science* **358** (6362), 511–513.

FAN, H., HEIRANIAN, M. & ELIMELECH, M. 2024 The solution-diffusion model for water transport in reverse osmosis: What went wrong? *Desalination* **580**, 117575.

FAUCHER, S. *et al.* 2019 Critical knowledge gaps in mass transport through single-digit nanopores: a review and perspective. *J. Phys. Chem. C* **123** (35), 21309–21326.

FENG, J., LIU, K., GRAF, M., DUMCENCO, D., KIS, A., DI VENTRA, M. & RADENOVIC, A. 2016 Observation of ionic coulomb blockade in nanopores. *Nat. Mater.* **15** (8), 850–855.

FOGLIA, F., FRICK, B., NANIA, M., LIVINGSTON, A.G. & CABRAL, J.T. 2022 Multimodal confined water dynamics in reverse osmosis polyamide membranes. *Nat. Commun.* **13** (1), 2809.

FORNASIERO, F., PARK, H.G., HOLT, J.K., STADERMANN, M., GRIGOROPOULOS, C.P., NOY, A. & BAKAJIN, O. 2008 Ion exclusion by sub-2-nm carbon nanotube pores. *Proc. Natl Acad. Sci.* **105** (45), 17250–17255.

FUJIOKA, T., OSHIMA, N., SUZUKI, R., PRICE, W.E. & NGHIEM, L.D. 2015 Probing the internal structure of reverse osmosis membranes by positron annihilation spectroscopy: gaining more insight into the transport of water and small solutes. *J. Memb. Sci.* **486**, 106–118.

FUMAGALLI, L. *et al.* 2018 Anomalously low dielectric constant of confined water. *Science* **360** (6395), 1339–1342.

GEISE, G.M. 2022 Bridging membrane transport models. *Science* **377** (6602), 152–152.

GREENLEE, L.F., LAWLER, D.F., FREEMAN, B.D., MARROT, B. & MOULIN, P. 2009 Reverse osmosis desalination: water sources, technology, and today's challenges. *Water Res.* **43** (9), 2317–2348.

HEGDE, V.H., DOHERTY, M.F. & SQUIRES, T.M. 2022 A two-phase model that unifies and extends the classical models of membrane transport. *Science* **377** (6602), 186–191.

HEIRANIAN, M., TAQIEDDIN, A. & ALURU, N.R. 2020 Revisiting Sampson's theory for hydrodynamic transport in ultrathin nanopores. *Phys. Rev. Res.* **2** (4), 043153.

JANSSEN, M., HÄRTEL, A. & VAN ROIJ, R. 2014 Boosting capacitive blue-energy and desalination devices with waste heat. *Phys. Rev. Lett.* **113** (26), 268501.

JENSEN, K.H., VALENTE, A.X.C.N. & STONE, H.A. 2014 Flow rate through microfilters: influence of the pore size distribution, hydrodynamic interactions, wall slip, and inertia. *Phys. Fluids* **26** (5), 052004.

JORGENSEN, W.L., CHANDRASEKHAR, J., MADURA, J.D., IMPEY, R.W. & KLEIN, M.L. 1983 Comparison of simple potential functions for simulating liquid water. *J. Chem. Phys.* **79** (2), 926–935.

JOUNG, I.S. & CHEATHAM, T.E. 2008 Determination of alkali and halide monovalent ion parameters for use in explicitly solvated biomolecular simulations. *J. Phys. Chem. B* **112** (30), 9020–9041.

KÄSTNER, J. 2011 Umbrella sampling. *Wiley Interdisciplinary Rev.: Comput. Mol. Sci.* **1** (6), 932–942.

KAVOKINE, N., MARBACH, S., SIRIA, A. & BOCQUET, L. 2019 Ionic Coulomb blockade as a fractional Wien effect. *Nat. Nanotechnol.* **14** (6), 573–578.

KAVOKINE, N., NETZ, R.R. & BOCQUET, L. 2021 Fluids at the nanoscale: from continuum to subcontinuum transport. *Annu. Rev. Fluid Mech.* **53** (1), 377–410.

LANGER, J.S. 1969 Statistical theory of the decay of metastable states. *Annal. Phys-New York* **54** (2), 258–275.

LI, H., WANG, S., ZHENG, J. & WANG, J. 2024*a* Electric field modulation of water transport in carbon nanotubes: insights from molecular dynamics simulations. *J. Phys. Chem. C* **128** (49), 21190–21200.

LI, S., ZHANG, X., LIU, Y. & SU, J. 2022 Asymmetric transport and desalination in graphene channels. *Phys. Chem. Chem. Phys.* **24** (21), 13245–13255.

https://doi.org/10.1017/jfm.2025.10961 Published online by Cambridge University Press

LI, Z., HALL, A.T., WANG, Y., LI, Y., BYRNE, D.O., SCAMMELL, L.R., WHITNEY, R.R., ALLEN, F.I., CUMINGS, J. & NOY, A. 2024*b* Ion transport and ultra-efficient osmotic power generation in boron nitride nanotube porins. *Sci. Adv.* **10** (36), eado8081.

LU, C. *et al.* 2023 Dehydration-enhanced ion-pore interactions dominate anion transport and selectivity in nanochannels. *Sci. Adv.* **9** (27), eadf8412.

MACHA, M., MARION, S., NANDIGANA, V.V.R. & RADENOVIC, A. 2019 2D materials as an emerging platform for nanopore-based power generation. *Nat. Rev. Mater.* **4** (9), 588–605.

MASON, E.A. & LONSDALE, H.K. 1990 Statistical-mechanical theory of membrane transport. *J. Memb. Sci.* **51** (1–2), 1–81.

MONET, G., BOCQUET, M.-L. & BOCQUET, L. 2023 Unified non-equilibrium simulation methodology for flow through nanoporous carbon membrane. *J. Chem. Phys.* **159** (1), 014501.

NICKERSON, T.R., ANTONIO, E.N., MCNALLY, D.P., TONEY, M.F., BAN, C. & STRAUB, A.P. 2023 Unlocking the potential of polymeric desalination membranes by understanding molecular-level interactions and transport mechanisms. *Chem. Sci.* **14** (4), 751–770.

OTERO, J.A., MAZARRASA, O., VILLASANTE, J., SILVA, V., PRÁDANOS, P., CALVO, J.I. & HERNÁNDEZ, A. 2008 Three independent ways to obtain information on pore size distributions of nanofiltration membranes. *J. Memb. Sci.* **309** (1), 17–27.

PARK, H.B., KAMCEV, J., ROBESON, L.M., ELIMELECH, M. & FREEMAN, B.D. 2017 Maximizing the right stuff: the trade-off between membrane permeability and selectivity. *Science* **356** (6343), eaab0530.

PARSEGIAN, A. 1969 Energy of an ion crossing a low dielectric membrane: solutions to four relevant electrostatic problems. *Nature* **221** (5183), 844–846.

PAUL, D.R. 1973 Relation between hydraulic permeability and diffusion in homogeneous swollen membranes. *J. Polym. Sci.: Polym. Phys. Ed.* **11** (2), 289–296.

QASIM, M., BADRELZAMAN, M., DARWISH, N.N., DARWISH, N.A. & HILAL, N. 2019 Reverse osmosis desalination: a state-of-the-art review. *Desalination* **459**, 59–104.

RADHA, B. *et al.* 2016 Molecular transport through capillaries made with atomic-scale precision. *Nature* **538** (7624), 222–225.

RICHARDS, L.A., SCHÄFER, A.I., RICHARDS, B.S. & CORRY, B. 2012*a* The importance of dehydration in determining ion transport in narrow pores. *Small* **8** (11), 1701–1709.

RICHARDS, L.A., SCHÄFER, A.I., RICHARDS, B.S. & CORRY, B. 2012*b* Quantifying barriers to monovalent anion transport in narrow non-polar pores. *Phys. Chem. Chem. Phys.* **14** (33), 11633–11638.

ROBIN, P. *et al.* 2023 Long-term memory and synapse-like dynamics in two-dimensional nanofluidic channels. *Science* **379** (6628), 161–167.

ROBIN, P., KAVOKINE, N. & BOCQUET, L. 2021 Modeling of emergent memory and voltage spiking in ionic transport through angstrom-scale slits. *Science* **373** (6555), 687–691.

SAHU, S., DI VENTRA, M. & ZWOLAK, M. 2017 Dehydration as a universal mechanism for ion selectivity in graphene and other atomically thin pores. *Nano Lett.* **17** (8), 4719–4724.

SARBOLOUKI, M.N. & MILLER, I.F. 1973 On pore flow models for reverse osmosis desalination. *Desalination* **12** (3), 343–359.

SECCHI, E., MARBACH, S., NIGUÈS, A., STEIN, D., SIRIA, A. & BOCQUET, L. 2016 Massive radius-dependent flow slippage in carbon nanotubes. *Nature* **537** (7619), 210–213.

SHI, D., WANG, W., LIANG, Y., DUAN, L., DU, G. & XIE, Y. 2023 Ultralow energy consumption Angstrom-Fluidic memristor. *Nano Lett.* **23** (24), 11662–11668.

SIRIA, A., PONCHARAL, P., BIANCE, A.-L., FULCRAND, R., BLASE, X., PURCELL, S.T. & BOCQUET, L. 2013 Giant osmotic energy conversion measured in a single transmembrane boron nitride nanotube. *Nature* **494** (7438), 455–458.

STRAUB, A.P., OSUJI, C.O., CATH, T.Y. & ELIMELECH, M. 2015 Selectivity and mass transfer limitations in pressure-retarded osmosis at high concentrations and increased operating pressures. *Environ. Sci. Technol.* **49** (20), 12551–12559.

SU, Z., CHEN, J., ZHAO, Y. & SU, J. 2019 How ions block the single-file water transport through a carbon nanotube. *Phys. Chem. Chem. Phys.* **21** (21), 11298–11305.

TAKEUCHI, H., TANAKA, H., NGHIEM, L.D. & FUJIOKA, T. 2018 Emerging investigators series: a steric pore-flow model to predict the transport of small and uncharged solutes through a reverse osmosis membrane. *Environ. Sci.: Water Res. & Technol.* **4** (4), 493–504.

THOMPSON, A.P. *et al.* 2022 Lammps-a flexible simulation tool for particle-based materials modeling at the atomic, meso, and continuum scales. *Comput. Phys. Commun.* **271**, 108171.

TUNUGUNTLA, R.H., HENLEY, R.Y., YAO, Y.-C., PHAM, T.A., WANUNU, M. & NOY, A. 2017 Enhanced water permeability and tunable ion selectivity in subnanometer carbon nanotube porins. *Science* **357** (6353), 792–796.



https://doi.org/10.1017/jfm.2025.10961 Published online by Cambridge University Press

WANG, A. *et al.* 2024 Selective ion transport through hydrated micropores in polymer membranes. *Nature* 1–6.
WANG, L., CAO, T., DYKSTRA, J.E., PORADA, S., BIESHEUVEL, P.M. & ELIMELECH, M. 2021 Salt and water transport in reverse osmosis membranes: beyond the solution-diffusion model. *Environ. Sci. Technol.* **55** (24), 16665–16675.
WANG, L., HE, J., HEIRANIAN, M., FAN, H., SONG, L., LI, Y. & ELIMELECH, M. 2023 Water transport in reverse osmosis membranes is governed by pore flow, not a solution-diffusion mechanism. *Sci. Adv.* **9** (15), eadf8488.
WANG, R. & LIN, S. 2021 Pore model for nanofiltration: History, theoretical framework, key predictions, limitations, and prospects. *J. Memb. Sci.* **620**, 118809.
WIJMANS, J.G. & BAKER, R.W. 1995 The solution-diffusion model: a review. *J. Memb. Sci.* **107** (1–2), 1–21.
XIE, Y., SHI, D., WANG, W. & WANG, Z. 2023 Surface-charge governed ionic blockade in Angstrom-scale latent-track channels. *Nanoscale* **15** (21), 9560–9566.
XU, J., ZHU, C., WANG, Y., LI, H., HUANG, Y., SHEN, Y., FRANCISCO, J.S., ZENG, X.C. & MENG, S. 2019 Water transport through subnanopores in the ultimate size limit: Mechanism from molecular dynamics. *Nano Res.* **12** (3), 587–592.
YAO, Y. *et al.* 2024 More resilient polyester membranes for high-performance reverse osmosis desalination. *Science* **384** (6693), 333–338.
YONG, H., HE, X. & MERLITZ, H. 2022 Connection between intrapore free energy, molecule permeation, and selectivity of nanofiltration membranes. *Macromolecules* **55** (10), 4119–4133.
YOU, Y., ISMAIL, A., NAM, G.-H., GOUTHAM, S., KEERTHI, A. & RADHA, B. 2022 Angstrofluidics: walking to the limit. *Annu. Rev. Mater. Res.* **52** (1), 189–218.
ZHAN, C., AYDIN, F., SCHWEGLER, E., NOY, A. & PHAM, T.A. 2020 Understanding cation selectivity in Carbon nanopores with hybrid first-principles/Continuum simulations: implications for water desalination and separation technologies. *ACS Appl. Nano Mater.* **3** (10), 9740–9748.
ZHANG, S., FU, L. & XIE, Y. 2024 Counterion blockade in a heterogeneously charged single-file water channel. *J. Phys. Chem. B* **128** (38), 9206–9212.
ZHANG, X., WEI, M., XU, F. & WANG, Y. 2020 Pressure-dependent ion rejection in nanopores. *J. Phys. Chem. C* **124** (37), 20498–20505.
ZHANG, Z., WEN, L. & JIANG, L. 2021 Nanofluidics for osmotic energy conversion. *Nat. Rev. Mater.* **6** (7), 622–639.
ZHOU, K. & XU, Z. 2020 Ion permeability and selectivity in composite nanochannels: engineering through the end effects. *J. Phys. Chem. C* **124** (8), 4890–4898.
ZHOU, W. & SONG, L. 2005 Experimental study of water and salt fluxes through reverse osmosis membranes. *Environ. Sci. Technol.* **39** (9), 3382–3387.
ZUO, K., WANG, W., DESHMUKH, A., JIA, S., GUO, H., XIN, R., ELIMELECH, M., AJAYAN, P.M., LOU, J. & LI, Q. 2020 Multifunctional nanocoated membranes for high-rate electrothermal desalination of hypersaline waters. *Nat. Nanotechnol.* **15** (12), 1025–1032.

https://doi.org/10.1017/jfm.2025.10961 Published online by Cambridge University Press